


## Article

# Influence of Chloride/Iodide Ratio in $\text{MAPbI}_{3-x}\text{Cl}_x$ Perovskite Solar Devices: Case of Low Temperature Processable AZO Sub-Layer

Manon Spalla <sup>1,2</sup>, Lara Perrin <sup>1,\*</sup> , Emilie Planès <sup>1</sup>, Muriel Matheron <sup>2</sup> , Solenn Berson <sup>2</sup> and Lionel Flandin <sup>1</sup> 

<sup>1</sup> Department LEPMI/GUIDE, Université Grenoble Alpes, Université Savoie Mont Blanc, CNRS, Grenoble INP, LEPMI, 38000 Grenoble, France

<sup>2</sup> Department CEA/LITEN/INES, Université Grenoble Alpes, CEA, 73375 Le Bourget du Lac, France

\* Correspondence: lara.perrin@univ-smb.fr

Received: 6 March 2020; Accepted: 9 April 2020; Published: 14 April 2020



**Abstract:** A significant current challenge for perovskite solar technology is succeeding in designing devices all by low temperature processes. This could help for both rigid devices industrialisation and flexible devices development. The depositions of nanoparticles from colloidal suspensions consequently emerge as attractive approaches, especially due to their potential for low temperature curing not only for the photoactive perovskite layer but also for charge transporting layers. Here, NIP solar cells based on aluminium doped zinc oxide (AZO) electron transport layer were fabricated using a low temperature compatible process for AZO deposition. For the extensively studied perovskites based on methylammonium lead halides ( $\text{MAPbI}_{3-x}\text{Cl}_x$ ), the chloride/iodide equation is widely proposed to follow an optimal value corresponding to an introduced MAI:PbCl<sub>2</sub> ratio of 3:1. However, the perovskite formulation should be considered as a key parameter for the optimization of power conversion efficiency when exploring new perovskite sub-layers. We here propose a systematic method for the structural determination of the optimal ratio. It may depend on the sublayer and results from structural changes around the optimal value. The functional properties gradually increase with the addition of chlorine as long as it remains intercalated in a single phase. Above the optimal ratio, the appearance of two phases degrades the system.

**Keywords:** chloride/iodide ratio; low temperature processable AZO;  $\text{MAPbI}_{3-x}\text{Cl}_x$  perovskite

## 1. Introduction

Over the last ten years, the field of photovoltaics has indubitably been reversed by a third generation of photovoltaics based on perovskite solar cells (PSC). Organic–inorganic lead halide perovskites are an ideal and competitive candidate because of their well-adapted opto-electronic properties such as a high carrier diffusion length [1] and the weak binding energy of their excitons [2]. PSCs have even shown very promising results, with performance levels up to 25% [3]. Despite this high potential, photovoltaic efficiency of PSCs is extremely dependent on their detailed design, especially for the materials selected as charge extracting layers. Among effects induced by the electron and hole transporting layers, the influence of the perovskite sub-layer nature (chemistry and/or morphology) on the perovskite material is a key feature. It is a sensitive parameter difficult to control and understand [4]. In addition, the development of devices compatible with low temperature processes receive an important consideration from present developed research activities, and the development of compatible materials still remains a major challenge. Developing a perovskite formulation compatible with low temperature processable architectures is thus of great interest. In major architectures under development, the perovskite layer is

deposited on a  $\text{TiO}_2$  electron transporting layer (ETL) [5,6], and the mesoporous form of  $\text{TiO}_2$  is the most commonly employed to reach performance levels greater than 20% [7,8]. However, this form is not affordable using low temperature processes, and thus not compatible with the development of flexible applications, tandem solar cells or large-scale commercialization.

Alternatives should thus be considered, keeping in mind that the perovskite sub-layer nature directly affects the perovskite microstructure.  $\text{TiO}_2$  traditional electron transport layer is not very powerful for charge extraction at its interface, peculiarly in planar structure affordable using low temperature process. Moreover,  $\text{TiO}_2$  based devices are known to suffer from critical deterioration under ultraviolet illumination. Several studies have already been conducted with other metal oxides compatible with low temperature processes, specifically  $\text{ZnO}$  [9,10] and  $\text{SnO}_2$  [11,12].  $\text{SnO}_2$  demonstrated a great transmission rate and an elevated electron mobility, with adapted energy band gap and relatively deep conduction band level. These properties lead to an efficient ability for extraction and transport of electrons, thus reducing the accumulation of charges at the perovskite/ETL interface. To increase the charges' transfer efficiency, several dopants (for instance: Li, Mg, Y, Sb, Nb, Sb, Al, Ga, etc.) have also been added in order to maximize the conductivity without affecting the transmission. In addition, many low cost and low energy consumption roads are affordable to fabricate  $\text{SnO}_2$  nanomaterials, and they can easily be processed by low-temperature methods ( $<200^\circ\text{C}$ ). The use of  $\text{SnO}_2$  as efficient electron transporting layer for perovskite devices has now largely been studied and is the subject of numerous reviews [13–15]. As regards  $\text{ZnO}$ , developed systems showed poor stability [16], and the attention has now shifted to aluminum doped  $\text{ZnO}$  (AZO) [17–19], that results in a more stable interface with perovskite [20]. Aluminium doping also causes a shift in energy of the Fermi level towards the conduction band, thus reducing AZO work function [21]. Carrier concentration and electron mobility are also increased, improving the conductivity of the material. Thus, AZO has superior optical and electrical properties compared to that of  $\text{TiO}_2$  [22]. Although AZO is sparsely studied [19,22], recent articles concerning its application have demonstrated its advantages and potential for high performances [23]. Accordingly, this paper focuses on solar cells involving an aluminium doped zinc oxide electron transport layer manufactured using nanoparticle deposition from colloidal suspension and low temperature curing.

In order to optimize the performances of perovskite deposited on this little documented AZO layer, we present here a careful study of the influence of the introduced chloride proportion in a  $\text{MAPbI}_{3-x}\text{Cl}_x$  mono-cation perovskite formulation (MA = methylammonium  $\text{CH}_3\text{NH}_3^+$ ). One of the primary objectives of this study is to develop a low-temperature manufacturing process fully adaptable to flexible substrates. We also investigate its impact on the perovskite layer and device performances. The present study thus focuses on the most well-known and studied perovskite form, the so-called MAPI. Indeed, although alternative structures with different combinations of organic cations, metallic cations and halogenated anions are day-to-day developed in search of performance perfection [24,25], recent works have demonstrated the potential of this pioneer perovskite to provide relevant devices simultaneously stable and performing [26]. However, a literature survey suggests that, in order to be compatible with an easy to scale up process in "one-step", the MAPI perovskite should contain a certain amount of chloride. Because of the required usage of chlorinated precursors to optimize the performance of these PSCs, it should be referred to as  $\text{MAPbI}_{3-x}\text{Cl}_x$  [27]. Its ability to showcase improved performances originates from several phenomena, mainly involving an optimization of the active layer crystallinity together with preferential crystalline orientations [28,29], and a defects passivation by  $\text{PbCl}_2$  at grain boundaries which limits the recombination rate [30,31]. Furthermore, the addition of chloride in the formulation of PSCs may enhance the electronic properties, depending on the nature of the layer on which the perovskite is deposited. For instance, in the case of perovskite deposition on a  $\text{TiO}_2$  surface, favorable chloride–titanium interactions were proved to occur at the interface, resulting in a curvature of the conduction band and allowing for better charge collection [32,33]. This example complements the previously mentioned potential for dependency of the perovskite properties depending on the nature of its sub-layer, herein ETL. In this work, a comprehensive study

of the impact of chloride ratio in  $\text{MAPbI}_{3-x}\text{Cl}_x$  perovskite microstructure and performance is detailed in order to develop an adapted formulation for specific AZO layers.

The  $\text{MAPbI}_{3-x}\text{Cl}_x$  formulation was gradually varied by manipulating the MAI:PbCl<sub>2</sub> ratio, and the effect on the perovskite structure of both chloride/iodide ratio and methylamine in excess is identified and discussed. If, in first instance, this study could sound redundant with investigations already conducted in literature essentially on TiO<sub>2</sub>-based perovskite devices [30,34]; a manifest proof that this problematic is not behind the times will be here provided. Indeed, an optimal chloride ratio, specific to AZO substrates and different from the one generally used in literature for the common TiO<sub>2</sub> based devices and often considered as a stoichiometric result, is here brought to light. Furthermore, in these recent times, the study of the optimal  $\text{MAPbI}_{3-x}\text{Cl}_x$  formulation according the sublayer nature seems to gain in interest especially regarding low temperature processed PSCs. These includes, for example, works from Tombe et al. on ITO/PEDOT/ $\text{MAPbI}_{3-x}\text{Cl}_x$ /PCBM/Al architecture for which an optimal composition different from the traditional one on TiO<sub>2</sub> was also found [35], or fresh other works from Mehdi et al. on ITO/SnO<sub>2</sub>/ $\text{MAPbI}_{3-x}\text{Cl}_x$ /P3HT/Au architecture [36].

To complete our AZO-based solar devices, a P layer based on poly (3-hexyl thiophene) P3HT was selected to obtain a NIP architecture. Indeed, the latter possesses a well-known morphology and adequate optoelectronic properties [37] to provide workable [38] and stable [39] PSC devices. In addition, P3HT is known to possess an adequate thermal stability and to be able to act as protective layer against oxygen and moisture permeation, while keeping a reasonable cost [40]. Diverse compounds have however already been proposed as a hole transporting layer (HTL): these could be inorganic materials, organic semi-conducting molecular or polymeric materials [41]. Inorganic HTL generally possess very good properties with high hole mobilities, but compounds compatible with low temperature processes (for instance: CuSCN, CuI, NiO) are mainly soluble in solvents that are at least a bit destructive for perovskite, leading to consequences on stability [41,42]. Regarding the molecular Spiro-OMeTAD (2,2',7,7'-tetrakis[N,N-di(4-methoxyphenyl)amino]-9,9'-spirobifluorene) which is the most often used HTL: if it enables to reach high performances, the stability of resulting photovoltaic devices is very low especially under temperature stress [43], thus hindering their industrialization. Otherwise, conductive polymers generally possess simultaneously helpful solubility, adequate stability, and high charge carrier mobility. P3HT even possesses an excellent hole mobility up to  $0.2 \text{ cm}^2 \text{ V}^{-1} \text{ s}^{-1}$  [44,45]. As to date, standard use of P3HT can afford efficiencies up to 16% in mesoscopic PSCs after molecular weight optimization [46], doping strategies allowed to reach 19% PCE [40], and recently the addition of an interlayer allowed to achieve efficiencies above 22% [45] which definitely establish the high potential of P3HT.

This paper is thus focused on a quite simple and easy processable ITO/AZO/ $\text{MAPbI}_{3-x}\text{Cl}_x$ /P3HT/Au architecture and the present study was conducted using a full set of characterization tools (X-ray diffraction, UV-Visible absorption, photoluminescence, infrared spectroscopy, and potentiometric titration) correlated with the evaluation of the photovoltaic parameters.

## 2. Materials and Methods

**Preparation of perovskite precursors.** All the solutions prepared and mentioned in this section were fabricated and kept in a nitrogen-filled glove box. Methylamine iodide ( $\text{CH}_3\text{NH}_3\text{I}$ ) was purchased from Lumtech, with a 99.9% purity degree. The solvent used to dissolve the powder is anhydrous N,N-dimethylformamide (Sigma-Aldrich, degree of purity 99.8%) and the final concentration of the methylamine solution was 4.8 M. The perovskite precursors solutions with varying chloride contents were prepared by mixing lead chloride (Sigma Aldrich, degree of purity 99.9%) with the freshly prepared methylamine solution and additional DMF, using the necessary molar ratio (see Table 1). The solutions of pure  $\text{MAPbI}_3$  and  $\text{MAPbCl}_3$  perovskites were respectively prepared by dissolving lead iodide (Sigma Aldrich, degree of purity 99.9%) with the methylamine iodide solution, or by dissolving lead chloride and methylamine chloride (Sigma Aldrich, purity degree of 98%) in DMSO. The final solutions were then stirred at room temperature for three hours. In order to adapt all thicknesses at

about 300 nm, it was necessary to adjust and reduce the concentrations of the mother solutions by adding DMF.

**Table 1.** Composition details of the perovskites' mother solutions (volume = 2.5mL).

Sample	MAI (g)	MAcI (g)	PbI <sub>2</sub> (g)	PbCl <sub>2</sub> (g)
MAPbCl <sub>3</sub>	-	0.150	-	0.618
MAPbI <sub>3</sub>	0.356	-	1.024	-
PK 2-1	0.712	-	-	0.618
PK 3-1	1.068	-	-	0.618
PK 4-1	1.424	-	-	0.618
PK 5-1	1.777	-	-	0.618

Fabrication of perovskite devices. Glass/ITO substrates were sequentially washed with acetone, 2-propanol and deionized water, before to be dried at 100 °C for 30 min. The following steps were then realized in a nitrogen-filled glove box. An aluminum doped zinc oxide nanoparticles suspension (2.5 wt% in 2-propanol, purchased from Avantama) was then spin-coated at 1000 rpm for 1 min and at 2000 rpm for 30 seconds before to be annealed at 80 °C for 1 min to form the ETL layer. This layer was then treated with 30 minutes of UV-Ozone [20]. The perovskite precursor solutions were filtered before use (45 µm) and spin-coated on cooled down substrates in order to afford a thickness close to 300 nm. The substrates were then annealed at 100 °C for one minute, followed by the spin-coating of a 15 mg/mL chlorobenzene solution of P3HT (poly 3-hexylthiophene, purchased from Sigma-Aldrich) as HTL. The spin-coating was made in two phases: 1500 rpm for 40 seconds for spreading, followed by 2000 rpm for 30 seconds for drying. Finally, gold electrodes were deposited by evaporation under a  $1.10^{-6}$  bar vacuum to finalize the device fabrication.

Potentiometric titration. The reaction of AgNO<sub>3</sub> with I<sup>-</sup> and Cl<sup>-</sup> leads to the formation of silver iodide or silver chloride. The evolution of this reaction can be monitored with potentiometric measurements. Iodide will first react with AgNO<sub>3</sub> and when all I<sup>-</sup> present in the solution will have been consumed, the chloride will react with AgNO<sub>3</sub>. Two different drops will appear on the curve, each of them corresponding to the consumption of a specific halide. The calculation of the ratio between the two equivalent volumes obtained allows an estimation of the chloride ratio inside the perovskite samples. Solutions and samples preparation: all experiments were made in ultra-pure water. In order to adapt the AgNO<sub>3</sub> concentration range, an estimation of the halogen content was made using the following approximations: density of the perovskite considered close to 1 g/cm<sup>3</sup> and perovskite volume equal to the thickness of the layer multiplied by the surface area (250 nm × 17 mm × 25 mm). This allowed us to get an order of magnitude of the halogen concentration and the choice of the titrant solution concentration was then chosen accordingly (0.01 M). The chloride content being small and in order to shift its potentiometric end point and thus make the difference of iodide and chloride titrations well distinct, an additional controlled quantity of chloride was incorporated to the solution using a NaCl solution (0.001 M). The concentration of this solution was carefully chosen to get at least a 0.5 mL difference between the two-titration points, and its precise chloride content was first measured before being mixed with the samples solution. Perovskite samples were fabricated with the varying precursors ratio previously mentioned. The exact same kind of samples were used for the titration than for other characterizations. Six substrates were dissolved for each titration experiment. Electrodes: Two electrodes were used for this titration. The working electrode consisted in a silver wire and was dipping in the solution to titrate. The reference electrode was a Ag/AgCl electrode (KCl saturated) and was combined to a salt bridge filled with a saturated KNO<sub>3</sub> solution in order to avoid any interaction within the halogens present in the samples. Experiments: after dissolution of the six substrates in 25 mL of ultra-pure water in which 5 mL of the NaCl solution was added, the electrodes were connected to a Biologic-SP300 potentiostat and the evolution of potential was recorded using EC-lab software. A controlled rate (200 µL/min) of AgNO<sub>3</sub> solution was then added in the reactional mixture. Results

analysis: the obtained results allowed the calculation of the iodide and chloride contents in the solution. The consumption volumes of the  $\text{AgNO}_3$  by both halogens content are calculated as follows:

$$V_{\text{I}^-} = V_{\text{eq},1} \text{ and } V_{\text{Cl}^-} = V_{\text{eq},2} - V_{\text{eq},1} - V_{\text{Cl}^- \text{ from NaCl}}$$

with  $V_{\text{eq},2}$  being the consumption volume of  $\text{AgNO}_3$  by all halides present,  $V_{\text{eq},1}$  being the consumption volume of  $\text{AgNO}_3$  by  $\text{I}^-$ ,  $V_{\text{Cl}^- \text{ from NaCl}}$  being the consumption volume of  $\text{AgNO}_3$  by the content of  $\text{Cl}^-$  originated from incorporated NaCl. The chloride contents (%) inside the perovskite materials were then calculated as following  $= V_{\text{Cl}^-} / (V_{\text{Cl}^-} + V_{\text{I}^-})$ .

**Characterizations.** Photocurrent density vs. voltage (J-V) curves of solar cells were measured inside the glovebox with a scan speed of  $100 \text{ mV.s}^{-1}$  using a Keithley source meter unit (model 2400) and an AM1.5G ( $100 \text{ mW.cm}^{-2}$ ) solar simulator. A bias scan from 2.5 V to  $-0.2 \text{ V}$  was applied. The active area of each PSC cell was  $0.28 \text{ cm}^2$ . In order to eliminate artefacts due to differences in product batches and campaigns, all cells have been realized and measured within the same campaign. For all following characterizations, measurements were performed instantly after the samples exit from the glove box and conducted under atmospheric conditions, except infrared (IR) measurements which were conducted under nitrogen flow in order to allow longer acquisitions, and scanning electron microscopy (SEM), which is conducted under vacuum. SEM images were recorded using a field emission scanning electron microscope (Ultra 55 Zeiss, CMTC Platform-Grenoble INP). Kelvin probe measurements have been performed on representative AZO samples using a Scanning Kelvin Probe from KP Technologies. A 100 nm thick gold reference on a glass substrate was used. All X-Ray diffraction (XRD) patterns were acquired using  $\text{Co K}\alpha$  radiation as radiation source ( $\lambda = 1.79 \text{ \AA}$ ) across a  $2\theta = 0^\circ$  to  $90^\circ$  range (INEL). The results were converted with the Cu wavelength thanks to Bragg's law:  $\sin \theta_2 = (\lambda_2/\lambda_1) \sin \theta_1$ . The calculation of the relative crystallinity and phases' proportion was conducted as follows: normalization with ITO peak at  $29.9^\circ$  and then extraction of amorphous contribution and fit of each peak with a Gaussian law from  $0$  to  $33^\circ$ . Absorption spectra were obtained using a UV-visible spectrometer equipped with an integration sphere (Shimadzu UV-2600) in order to take into account the light scattering of the sample. Tauc plot method was used to evaluate the direct optical transitions. Photoluminescence (PL) spectra were measured using a fluorimeter (F-4500 Hitachi) at 550 nm excitation wavelength. In order to eliminate measurement artefacts, a low pass filter (595 nm) was placed in front of the excitation source and a high pass filter (600 nm) in front of the emission path of the sample. Infrared spectra were performed on a Spectrum One Perkin Elmer and were obtained with KBr-Perovskite mix tablets.

### 3. Results and Discussion

The characterizations of the  $\text{MAPbI}_{3-x}\text{Cl}_x$  perovskites were performed both on half-cells and complete cells, as shown in Figure 1. The half-cell structure will enable the intrinsic characterization of the perovskite layer by potentiometric titration, UV-Visible absorption, infrared spectroscopy, X-ray diffraction, and photoluminescence.

To alter the  $\text{MAPbI}_{3-x}\text{Cl}_x$  formulation, chloride is generally added through  $\text{PbCl}_2$  or  $\text{MACl}$ , or a combination of the two [47]. Both seem to play a similar role on the crystal orientation during the formation of perovskite [4,48]. Generally, the formulation also contains a  $\text{MA}^+$  rich environment, which favors a slower conversion of the perovskite film inducing a growth of crystalline domains during a further annealing step [27,49]. In most papers, the iodide fraction is brought using methylammonium iodide (MAI) and  $\text{PbCl}_2$  is the chloride source, typically in a 3:1 molar ratio [33,48–51]. In some cases, regrettably mostly limited to  $\text{TiO}_2$ -based devices, a validation of this optimal ratio has been realized. Here, in order to study the impact of the amount of chloride on the AZO-based perovskite microstructure, six different formulations were investigated: two “pure” perovskite formulations (leading to  $\text{MAPbI}_3$  and  $\text{MAPbCl}_3$ ) as well as four other formulations based on variable MAI:  $\text{PbCl}_2$  ratios. In addition to the 3:1 ratio, the ratios 5:1, 4:1, and 2:1 were thus also tested. The details of the



different perovskite formulations are shown in Table 2. This table additionally specifies the chloride amount introduced in the precursor solution and the real chloride amount finally present in the active layer. Both will be thereafter incorporated in all of the Figures of this paper, via double x-axis.

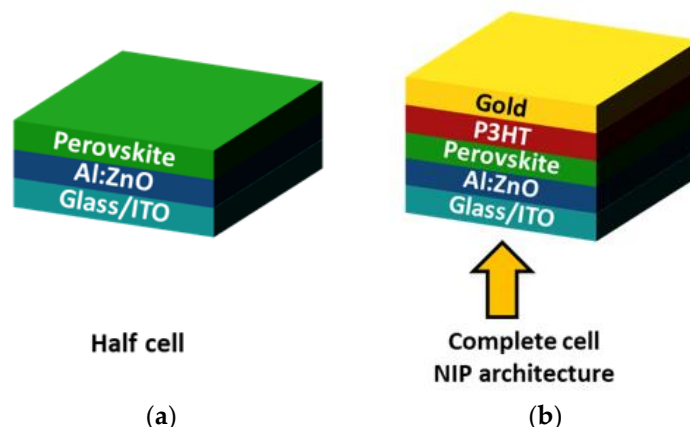


**Figure 1.** (a) Half cells architecture; (b) Complete photovoltaic (PV) cells architecture.

**Table 2.** Composition of studied perovskite precursor's solutions and corresponding J-V performances in aluminium doped zinc oxide (AZO)-based solar cells.

Acronym	MAPbCl <sub>3</sub>	PK 2-1	PK 3-1	PK 4-1	PK 5-1	MAPbI <sub>3</sub>
Precursors molar ratio	1 MAI 1 PbCl <sub>2</sub>	2 MAI 1 PbCl <sub>2</sub>	3 MAI 1 PbCl <sub>2</sub>	4 MAI 1 PbCl <sub>2</sub>	5 MAI 1 PbCl <sub>2</sub>	1 MAI 1 PbI <sub>2</sub>
Introduced chloride % Cl/(Cl + I)	100%	50%	40%	33%	28%	0%
Introduced MA excess (%)	0%	50%	67%	75%	80%	0%
Real chloride % (measured in the active layer)	100%	10%	30%	21%	17%	0%
Voc (mV)	Not measurable	414 ± 45	951 ± 12	920 ± 27	638 ± 100	Not measurable
Jsc (mA/cm <sup>2</sup> )	Not measurable	10.9 ± 1.2	11 ± 2.5	13 ± 3	2.2 ± 1.7	Not measurable
FF (%)	Not measurable	35 ± 2	58 ± 12	61 ± 5	89 ± 35	Not measurable
PCE (%)	Not measurable	1.6 ± 0.3	5.7 ± 0.8	7.2 ± 1.5	1.5 ± 1.6	Not measurable

Indeed, the optimization of PV performances cannot be performed without knowing the true amount of chloride present in the perovskite layer after both filtration of the precursors' solution (before the deposition of the layer) and after evaporation of some by-products (during the annealing step of the active layer, after the coating). To realize this study, the final halides proportion (chloride and iodide) was quantified by potentiometric titration using a standard argentometry method. A similar method has already been used and validated by Li et al. on perovskites [52]. An example of typical obtained curves, as well as a summary of the determined volumes for the equivalences of each synthesized perovskites, can be found at Figure S1 in Supporting Information.

The chloride content in the perovskite materials is here presented in Figure 2 as a function of the chloride content introduced into the precursors' solution, accompanied by a picture of the solutions. It is important to note that both the PK 4-1 solution and PK 5-1 solution are very clear. For PK 3-1, the solution was much more turbid, and the PK 2-1 solution being completely turbid along with an additional presence of a deposit at the bottom of the pillbox. The varying clarity of the different solutions is surprising as all solutions have the same amount of PbCl<sub>2</sub>, and it was not expected that the

more the introduced amount of MAI is high, the clearer the solution would be. It is known however that  $\text{PbCl}_2$  is poorly soluble in DMF but can form a soluble complex with MAI [53,54]. During the filtration step before deposition, a certain amount of insoluble  $\text{PbCl}_2$  can therefore be eliminated (filter with pore diameter of  $45\ \mu\text{m}$ ), the main part still present in solution being the complex formed between perovskite, DMF, and an amorphous chlorinated phase. Among the different present species,  $\text{MAI}$  is known to be formed during the perovskite deposition step and has the potential to partially sublime during annealing [47]. For the reasons stated, the chloride amount in the perovskite is lower than the level of chloride introduced with the precursors.

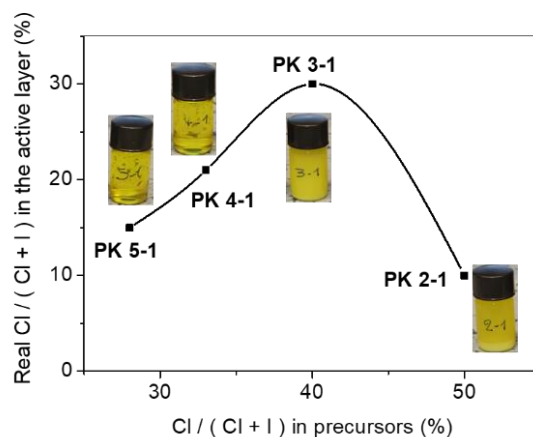


**Figure 2.** Relation between perovskite films and precursors solutions halide compositions (photographs of solutions before filtration are also presented).

The different perovskites were then tested in solar cell configuration. All cells and previous films were made with the same procedure, in particular the same annealing time. They have the same device architecture and a similar perovskite layer thickness close to 300 nm. The performance results will thus essentially depend on the composition of the perovskite layer. The obtained photovoltaic parameters are presented in Table 2, the corresponding J-V curves are displayed in Figure S2, and Figure S3 presents photographs of the respective perovskite layers.

PCE values here obtained are low but it is worth mentioning that AZO implementation in a NIP perovskite solar cell has rarely been characterized. Most studies involving AZO concern PIN structures, where AZO is the top layer [18,55]. Nevertheless, a few studies start describing photovoltaic devices with AZO as a bottom layer as well with performance levels up to 12% or 16% using respectively mono or multi-cation perovskites [22,23,56]. It should be also mentioned that thick AZO layers have already been directly used as transparent electrode, generally without electron transport layer thus showing that it can act as both electrode and ETL layers all-in-one [20]. Literature devices have been obtained using architectures and processing methods far from present work, for instance, using sputtering to achieve their AZO layer. This latter method is incompatible with a low-temperature process and is significantly different from the AZO nanoparticle deposition methodology here investigated. This specific AZO layer has however already proven its potential as ETL. The exact same commercial reference has been used with success in both organic and perovskite cells, but usually in inverted architectures [57–59]. In addition, other low temperature processed AZO materials made by completely different methods [60] have already been used as ETL in normal PSC architecture setups close to the one studied in this paper. Figure S4a presents SEM images of the here studied AZO nanoparticle layer, allowing to evaluate the obtained surface morphology. This specific ETL layer possesses a 4.2 eV work function, which has been checked using Scanning Kelvin Probe microscopy. This is lower than that generally obtained on other types of AZO but close to the value given by supplier and also close to standard  $\text{TiO}_2$  [61].

The scope of presented work is to study the potential of such a low temperature processable AZO bottom layer when using a one-step scalable perovskite process. As obtained photovoltaic performances may seem limited when compared to literature, it is first necessary to make a comparison with similar “planar” architectures such as  $\text{TiO}_2$ -compact/ $\text{MAPbI}_3$ /P3HT and our results are in good agreement since the latter also present performances close to 6–7% [38,62]. However, the present work should be considered as a first step in  $\text{AZO}_{\text{nanoparticle}}$  development as ETL sub-layer for perovskite devices, and several optimizations have still to be explored. First of all, the doping of P3HT could be a beneficial way [62–64], but the major issue to solve probably concerns the obtained perovskite films morphology (see SEM examples in Figure S4b,c) which probably suffers from a very rapid observed conversion (less than 1 min for all samples, see illustration in Figure S5).

As reported on Table 2, all our solar cells based on pure  $\text{MAPbCl}_3$  showed an ohmic behavior. This results from the chlorinated perovskite optoelectronic properties that prevents the absorption of light in the visible range (bandgap  $\sim 3$  eV useful for the photo-detectors applications [65]). The cells based on pure  $\text{MAPbI}_3$  here also demonstrated very low performances (nearly ohmic as well, see Figure S2). It should be mentioned that the good performances presented in literature with pure  $\text{MAPbI}_3$  either result from a “two steps” process [66] or from very different architectures [67–69]. In addition, a short window of a few minutes was here available on all our AZO-based devices for annealing optimization before perovskite deconversion, giving rapid performances degradation. The immediate  $\text{MAPbI}_3$  observed conversion on our AZO substrate can thus easily lead to fabrication defects like pinholes [70]. In order to counter this drawback, different thicknesses were tested in the recommended range [63] also without success. It seems thus that the AZO-based low-temperature process we here develop is not adapted to a pure  $\text{MAPbI}_3$  formulation. The incorporation of a  $\text{MA}^+$  excess seems thus vital. Indeed, a progressive sublimation of  $\text{MACl}$  is known to serve as regulating agent allowing a slower conversion [49], however it remains quite rapid in the presented AZO-system.

For cells based on  $\text{MAPbI}_{3-x}\text{Cl}_x$  (PK 2-1, PK 3-1, PK 4-1, and PK 5-1), the performances were found to be highly dependent on the  $\text{MAI}:\text{PbCl}_2$  ratio, with an optimal PCE of 7.2% obtained for the PK 4-1 formulation. Perovskites PK 2-1 and PK 5-1 display very low efficiencies, below 2%. This can be explained by very low values of open circuit tension ( $V_{oc}$ ) in the PK 2-1 formulation, whereas for the PK 5-1 formulation the limiting factor is the short circuit current ( $J_{sc}$ ). Even if it is known that  $\text{MA}$  excess can be eliminated through the  $\text{MACl}$  sublimation [47,68] (generated during the annealing step), PK 5-1 formulation contained too much  $\text{MA}$  and too little chloride for a possible transformation of all  $\text{MA}$  excess into  $\text{MACl}$ . A significant amount of  $\text{MAI}$  (not removable by annealing at  $100^\circ\text{C}$  [71]) should thus be present. When mixed with the perovskite, the non-photoactive  $\text{MAI}$  degrades the performances, and results in a relatively low value of  $J_{sc}$  ( $\sim 2 \text{ mA}/\text{cm}^2$ ). Regarding the PK 2-1 formulation, there is not enough iodine in the initial formulation to obtain a ratio of 3 iodine for 1 lead and form a perovskite with the  $\text{MAPbI}_3$  structure. However, as the final chloride content is then very low in the final perovskite, further investigations will be thus needed to understand how this formulation can result in a degraded  $V_{oc}$ .

For PK 3-1 formulation, the efficiency (5.7%) is sizable but lower than that obtained for PK 4-1 (7.2%). Given the corresponding introduced  $\text{Pb}:\text{I}$  ratio, the PK 3-1 usually recommended formulation seems to be theoretically the most appropriate formulation to lead to a  $\text{MAPbI}_3$  perovskite structure (with a possible sublimation release of 2  $\text{MACl}$  for 1  $\text{MAPbI}_3$ ) [72]. If this formulation has demonstrated its relevance on  $\text{TiO}_2$  substrates in literature, the results seems quite different here in the case of presented AZO substrate. The N layer has a strong impact on the microstructure of the obtained perovskite and different parameters could be implied: the chemical nature of the N layer material, its surface state possibly modified by additional treatments, and the perovskite induced annealing time. Adjusting the chloride ratio here proves to be a means of optimization.

In the following sections, we will try to evaluate the exact perovskite state in an AZO-based device according to the  $\text{MAI}:\text{PbCl}_2$  precursors ratio introduced. Indeed, the use of chlorinated precursors can present one drawback however: there is a risk for the formation of a purely chlorinated perovskite



phase,  $\text{MAPbCl}_3$ , which can be detrimental if present in large amounts, because of its unappropriated bandgap [73]. Furthermore, as suggested in literature [74], PSC performances are directly related to perovskite crystallinity. These two points can easily be evaluated by XRD analysis: Figure 3 presents results obtained from half-cells.

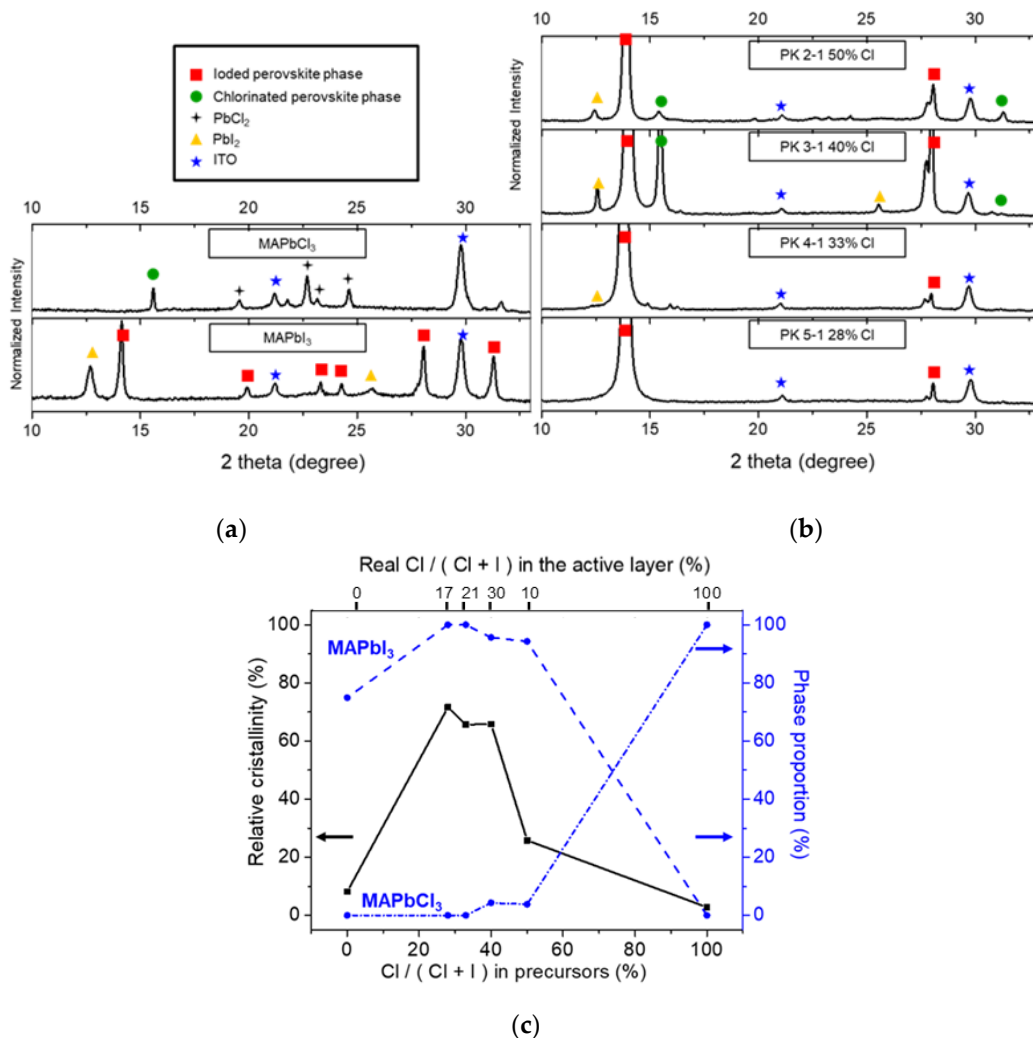


**Figure 3.** X-ray diffraction (XRD) diffractograms for (a) pure  $\text{MAPbCl}_3$  and  $\text{MAPbI}_3$ , (b) the perovskites obtained using different introduced Cl/I ratio; (c) Evolutions of both relative crystallinity and perovskite nature according to the halogen proportion.

The  $\text{MAPbCl}_3$  perovskite demonstrated a cubic lattice crystal structure at room temperature, in accordance to literature [75]. A preferred (100) orientation is visible on the XRD diffractogram of  $\text{MAPbCl}_3$  as also observed in literature [76]. The layer formed however is not optimal because traces of  $\text{PbCl}_2$  can be observed (reagent or degradation product). The intensity of peaks characteristic of the perovskite phase is rather weak, indicating a low level of crystallinity (the peaks related to ITO have a similar intensity). For the so-called "pure"  $\text{MAPbI}_3$  perovskite, the crystalline structure is tetragonal [77]. The two main crystalline orientations are (110) and (002). These are visible on the first order ( $14^\circ$ ): the two contributions are mixed in the same peak, as generally observed in literature [78]. These orientations are also observed at the second order (220) and (004) close to ( $28^\circ$ ) [4]. Other orientations are noticeable as well: (112) ( $20^\circ$ ), (211) ( $23^\circ$ ), (202) ( $24^\circ$ ), and (114) ( $31^\circ$ ) [78]. Some  $\text{PbI}_2$  is also present in large quantities (reagent or degradation product), suggesting non-optimized PV performances.

For the other perovskites synthesized using simultaneously chlorinated and iodized precursors, a structure with the preferred crystalline orientation (110) is formed (see Figure 3b), in accordance with the literature [4,79]. Two perovskite phases are noticed: the first one is the expected  $\text{MAPbI}_3$  phase and the second the  $\text{MAPbCl}_3$  phase. Their coexistence is not surprising considering the nature of the precursors used and how the observed phenomena has already been noticed in literature on other substrates [73,80]. In our study, the relative intensity of the chlorinated perovskite phase is dependent on the MAI:  $\text{PbCl}_2$  ratio. To quantify this result, the proportions of  $\text{MAPbI}_3$  and  $\text{MAPbCl}_3$  phases and the relative crystallinity of the photoactive layer were determined for all samples (see experimental section for details on the calculation and Figure 3c for their representation). First, we observe an increase of the  $\text{MAPbCl}_3$  phase for a chloride proportion introduced through the precursors' solution higher than 40%. As mentioned in literature [51,67,81], for a low chloride content, chloride atoms can be inserted into the main perovskite phase ( $\text{MAPbI}_3$ ), allowing for a preferential crystalline orientation and an increase in grain size. For high contents, it is here apparent that the insertion is no longer possible and  $\text{MAPbCl}_3$  is formed. PK 2-1 (introduced chloride content = 50%) is thus very particular because despite its low chloride content in the final perovskite (10%), it has a significant level of  $\text{MAPbCl}_3$ . This supports the fact that the intermediate complex has a determining role. Otherwise, the relative crystallinity is detected as optimal between 25% and 40% of introduced chloride. With Figure 3c, the optimal range could be thus highlighted if both parameters are taken into account, i.e., a highly crystalline layer combined with a low level of  $\text{MAPbCl}_3$  seems to be the best compromise. Therefore, the optimal chloride proportion corresponds to the PK 3-1 and 4-1 formulations (corresponding to an introduced chloride proportion between 33% and 40%, and a real chloride proportion between 21% and 30%). This is in agreement with the recorded PV performances as well, since PCE levels over 5% have been obtained for this range. Another parameter which is in accordance with a fact already noticed in literature [72] is that it seems that the optimal PCE could be related to the highest value obtained for the (110)/(220) ratio, related to  $14^\circ$  and  $28^\circ$ , respectively. Indeed, in our case the optimal PK 4-1 formulation possesses a (110)/(220) ratio about 5 times higher than the traditional PK 3-1 formulation.

The XRD results were strengthened by UV-visible absorption analyses, see Figure 4. Three optical transitions were identified in  $\text{MAPbI}_{3-x}\text{Cl}_x$  materials (PK 2-1, PK 3-1, PK 4-1, and PK 5-1). By comparing the results to that of pure perovskite materials, each transition was able to be attributed. The first transition at 765 nm (1.58 eV) is characteristic of the  $\text{MAPbI}_3$  perovskite and according to literature [82], it is related to the gap between the higher level of the first valence band and the lower level of the conduction band, which is the optical bandgap. The second transition at 500 nm (2.2 eV) originates from the lead–iodide octahedra [83] present in both the various perovskites and in  $\text{PbI}_2$ . Finally, the third transition visible at 400 nm (3.0 eV) is connected with the chlorinated perovskite phase [76].

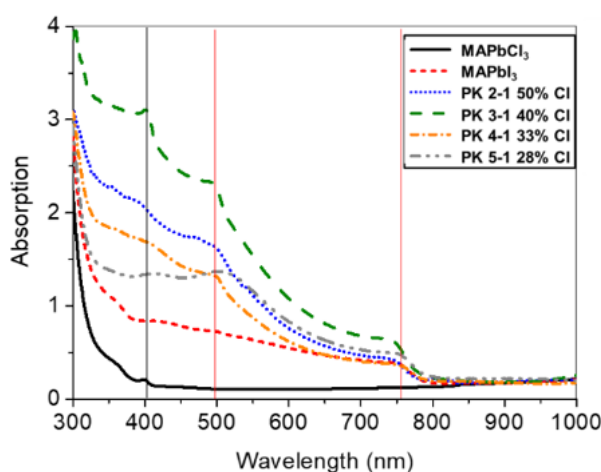


**Figure 4.** UV-visible absorption spectra of all fabricated perovskite films.

For all tested materials, few variations are observed in the onset of the first transition. Much larger variations are however observed for the other two transitions. The optical transition bandgap position located at about 2.2 eV (500 nm) is presented in Figure 5a versus the introduced chloride proportion. An increase in the bandgap was first noticed, followed by a stabilization between 33% and 40% of introduced chloride, and then a decrease. In literature [34], a modification of this transition can be observed in the case of a non-stoichiometric composition of the halogen-lead octahedra structure or here more convincing in the case of a chloride intercalation between units of  $\text{PbI}_6$  octahedra within the perovskite. In the case of a low chloride content, chloride intercalation within the  $\text{MAPbI}_3$  perovskite can possibly induce wider inclination angles between octahedral units, leading to a deformation of the electronic structure. Therefore, it can be here assumed that the energy level of this transition is directly related to the amount of chloride incorporated into the  $\text{MAPbI}_{3-x}\text{Cl}_x$  phase. Furthermore, the transition observed at 400 nm, in regards to the chlorinated phase, is evident for PK 2-1 and PK 3-1 formulations, which both present an important  $\text{MAPbCl}_3$  phase according to XRD results. These results support the proposed hypothesis that for a chloride introduced halogen proportion between 0 and 33%, a portion of chloride is incorporated into  $\text{MAPbI}_3$  and subsequently forms  $\text{MAPbI}_{3-x}\text{Cl}_x$ , which increases the 500 nm optical bandgap value. Above this ratio, the formation of a pure chlorinated perovskite phase seems to be favored to the detriment of the chloride insertion. This phase is clearly observable in XRD and UV-visible absorption analyses and its formation also implies a slight fall of the 500 nm second optical bandgap.

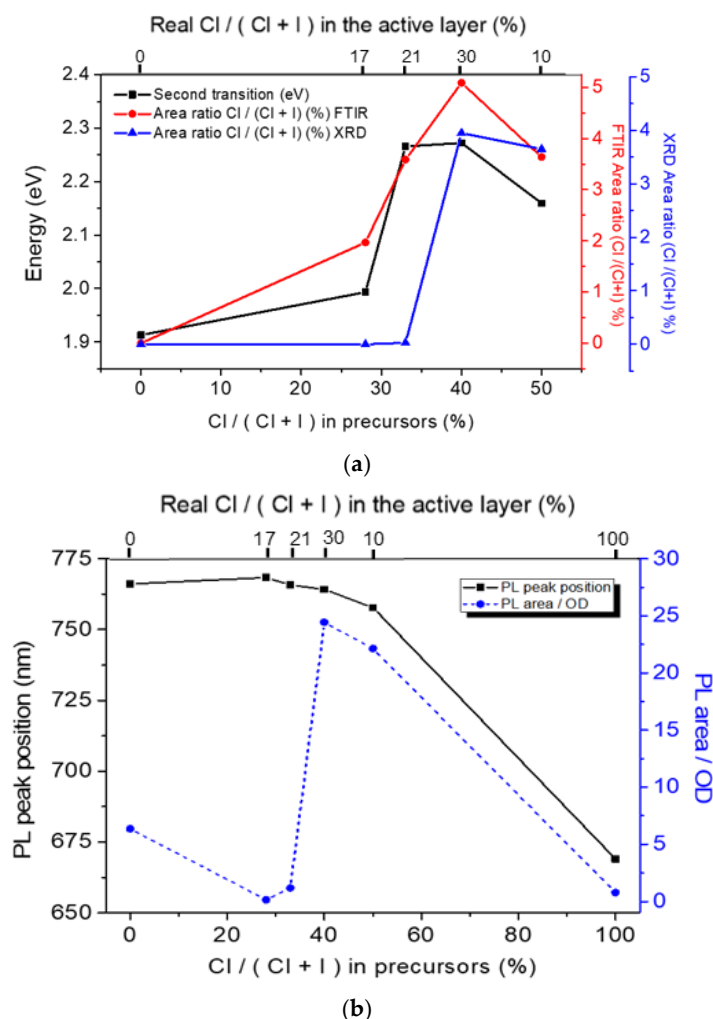


**Figure 5.** Evolution according to the chloride proportion of (a) the absorption second optical transition (left) and the chlorinated perovskite phase proportion (right: determined using either FTIR or XRD); (b) the PL emission (left:  $\lambda_{\text{em}}$  max, right: peak area normalized by OD at  $\lambda_{\text{ex}}$ ).

The UV-visible absorption spectrophotometry having allowed an analysis of the lead–iodide octahedral environment, a combination with another technique allowing to probe the environment of the organic cation seems to be relevant. The complete observation of the lead–iodide, lead–chloride, and cation environment bonds is possible using Raman spectroscopy in the 50 to 2000  $\text{cm}^{-1}$  range. However, in the case of perovskites, it is rather challenging to optimize the acquisition conditions in order to obtain a good signal-to-noise ratio while avoiding excessive soliciting of the sample [84]. An inappropriate use of the power laser can degrade the perovskite, which is additionally extremely sensitive to ambient conditions [85]. As such, this technique was not able to be used for our materials. Conversely, infrared spectroscopy sparsely used in the domain can be applied to perovskites and the 400 to 4000  $\text{cm}^{-1}$  range allows the study of the organic cation environment located at the center of the crystal lattice (CH, NH, and CN bonds).

Figure 6 shows the IR spectra in the 900–1700  $\text{cm}^{-1}$  relevant range, corresponding to band levels of the characteristic bonds present in the methylammonium cation environment of all studied perovskites in this paper. The most prevalent bands in the spectra correspond to the fundamental modes of the  $\text{MA}^+$  cation and its anharmonic contributions [86]. All bands in relation to the  $\text{NH}_3$  functional group are more intense than those in relation to the  $\text{CH}_3$  group. This is due to the location of the positive charge on the ammonium group which favors the variations of the dipole moments related to the vibrations of  $\text{NH}_3$  [87]. Referring to literature [87–89], the characteristic bands of the vibration modes of  $\text{MAPbI}_3$  and  $\text{MAPbCl}_3$  could be assigned and were confirmed by the IR spectra of the pure  $\text{MAPbI}_3$  and  $\text{MAPbCl}_3$  materials. To assess the presence of the initial reactants MAI and MACl in the perovskites, the IR spectra of the latter were also realized. From related spectra presented in Figure S6, it is evident that residues of the reactants are present however in very low quantities given the weak band intensities. A table outlining all peaks attributed to synthesized perovskites over the 400–4000  $\text{cm}^{-1}$  range is presented in Table S1. A shift of 10  $\text{cm}^{-1}$  can be observed between the two different observed perovskites for the majority of these bands. A possible explanation is due to the more electronegative nature of chlorine compared to iodine, which shifts the resonance vibration to a higher frequency [88]. The environment close to the organic cation, such as  $\text{Pb-X}_6$  octahedra, affects its modes of vibration.

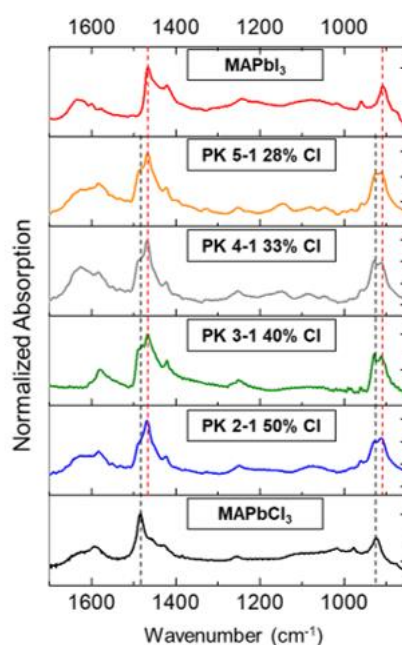


**Figure 6.** Infrared (IR) spectra of all fabricated perovskite materials (vertical dotted lines point out the difference between chlorinated and iodized perovskite materials).

For the IR spectra of the perovskites  $\text{MAPbI}_{3-x}\text{Cl}_x$ , double peaks were observed for some bands, especially at  $910$  and  $930\text{ cm}^{-1}$  and at  $1467$  and  $1484\text{ cm}^{-1}$ . The latter are identified in Figure 6 by black and red vertical dotted lines, corresponding to the  $\text{MAPbCl}_3$  and  $\text{MAPbI}_3$  phases, respectively. The relative proportions of these two phases can be determined by deconvolution of the double peaks, and Figure 5a thus presents an estimation of the  $\text{MAPbCl}_3$  content within the perovskite material (here determined using the  $910/930\text{ cm}^{-1}$  peaks). The same estimation obtained from XRD analyses is also presented in the same figure for comparison. The same trend is observed for both analyses. A simple shift is observed most likely due to the fact that IR spectroscopy allows probing of all phases in both  $\text{MAPbCl}_3$  and  $\text{MAPbI}_3$  contrary to XRD, which probes only the crystalline phases. It clearly appears that the chlorinated perovskite phase is limited up to an introduced chloride ratio of 33%. Below, the major phenomenon is an insertion of chloride atoms into the  $\text{Pb-I}_6$  octahedra (as denoted by the second transition increase). As the real chloride content of PK2-1 is strongly lower than the one introduced (10% vs. 50%), but its  $\text{MAPbCl}_3$  phase contribution is important, it is also clear that the perovskite intermediate may subsequently impose the chloride amounts incorporated within  $\text{MAPbI}_3$ .

Finally, the optoelectronic properties of these perovskites were characterized by photoluminescence spectroscopy: the obtained spectra are shown in Figure 7. For the purely chlorinated perovskite, a slight emission centered at  $670\text{ nm}$  was observed despite the imperceptible absorption of this material at the excitation wavelength, the value however corresponds to the emission reported in literature for  $\text{MAPbCl}_3$  [34]. For the mixed perovskites  $\text{MAPbI}_{3-x}\text{Cl}_x$ , it seems that PL analyses are more pertinent compared to UV-visible spectroscopy. Indeed, while there is no significant variation of the absorption optical bandgap at  $765\text{ nm}$ , a shift of the fluorescence emission peak is observed. The emission peak is close to  $765\text{ nm}$ , which is in accordance with the reported value in literature for the  $\text{MAPbI}_3$  phase [82]. For mixed perovskites, only the emission of the main phase ( $\text{MAPbI}_3$ ) can be observed. If a slight emission of the chlorinated phase would have been present, the latter should certainly be re-absorbed by  $\text{MAPbI}_3$ . The observed emission peak undergoes a blue shift for PK 2-1, this suggests an effect on the position of the conduction and valence bands in accordance with the observed change in  $V_{oc}$ . This shift cannot be due to the creation of additional defects which would induce a shift in the opposite direction instead [30]. A red shift is also observed for PK 5-1 whose formulation is rich in MAI. A residual amount of MAI must therefore be present in this formulation, which generates defects thus inducing the slight red shift observed. The described evolution of PL maximum peak with the chloride content is illustrated in Figure 5b.

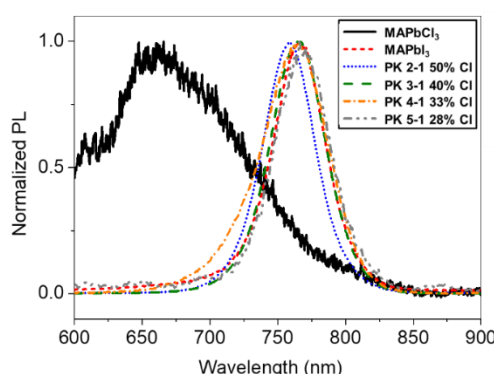


**Figure 7.** Normalized photoluminescence (PL) spectra of all synthesized perovskites (the analyses have been conducted on half-cells using a  $550\text{ nm}$  excitation wavelength).

The fluorescence intensity of the different synthesized perovskites was also studied (see Figure 5b): it was observed that PK 4-1 and PK 5-1 have weak fluorescence. For the PK 4-1 formulation, this is compatible with its good PV performances and indicates good charge transferability. As regards PK 5-1, the already detected excess of MAI in the material leads to a low diluted fluorescence yield, thus



inducing poor charge generation, clearly unfavorable for PV performances but not a priori incompatible with a good charge transferability. The PK 3-1 and PK 2-1 possess a very high fluorescence intensity, which signifies either a high level of defects inside the perovskite layer and/or a bad quenching at the N layer interface. This is most likely due to the non-negligible presence of the chlorinated perovskite phase (previously detected by XRD analyses) in these two formulations. In literature, the best performance levels are generally obtained for a PK 3-1 formulation (40% Cl introduced) [4,47,90], or even a PK 2-1 formation (50% Cl introduced) [34] on a  $\text{TiO}_2$  ETL. These results clearly emphasize the significance of the N-layer on the perovskite microstructure.

From the results and interpretations of the microstructural, physicochemical and physical analyses, the chloride addition mechanism in a  $\text{MAPbI}_3$  perovskite was able to be determined. On AZO-based substrate, chloride is first incorporated into the  $\text{MAPbI}_3$  structure, up to an optimal chloride content in precursors between 33% and 40% (Figure 5a). This range corresponds to the best PV performances obtained as well (Figure 8). The inserted chloride atoms allow for a preferential crystal growth resulting in the formation of larger and more crystalline domains (Figure 3c) with higher mobility and longer charge carrier lifetime [4]. For an introduced chloride content superior to 40%, it seems that the chlorinated perovskite is preferentially formed. The presence of this phase appears unfavorable for the PV mechanism because it does not participate in effective photon collection [76] and induces a high rate of radiative recombination observable in PL (Figure 5b).

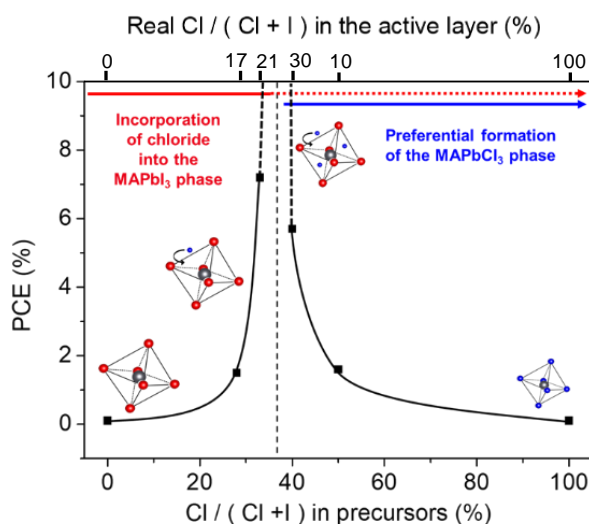


**Figure 8.** Evolution of PCE according to both chloride proportions (introduced and real). An extrapolation, understandable if there was no competition between the two mechanisms identified in blue and red caption, is presented in dotted line between 28 and 33% of Cl in the precursors' composition.

Consequently, for purposes of better controlling the microstructure and composition of the perovskite layer and therefore the performance of PSCs, it is decisive to optimize the chloride content in a  $\text{MAPbI}_3$  perovskite for each type of device architecture.

#### 4. Conclusions

The combination of appropriate and well-exploited characterizations has resulted in having a clear picture of the final material composition of the  $\text{MAPbI}_{3-x}\text{Cl}_x$  perovskite, when formed on an  $\text{AZO}_{\text{nanoparticle}}$  substrate. The main phase, involving  $\text{MAPbI}_3$ , contains chloride atoms incorporated within the crystal lattice, and the presence of an optimal ratio corresponding to maximized PV performance has been demonstrated. The presence of chloride is necessary in the development of efficient solar cells, but only if incorporated in small amounts into  $\text{MAPbI}_3$ , the formation of a pure

MAPbCl<sub>3</sub> phase being detrimental. Solar cells with excessive chloride levels, leading to the formation of MAPbCl<sub>3</sub>, lose efficiency.

In addition, it appears that the MAPbI<sub>3-x</sub>Cl<sub>x</sub> behavior on AZO is different from what is assumed in literature for TiO<sub>2</sub>. Thus, the formation process of perovskites seems extremely dependent on the bottom layer used. Referring to MAI: PbCl<sub>2</sub> perovskite initiators, a 3:1 ratio prescription is generally admitted on TiO<sub>2</sub> supporting substrates. However, a 4:1 optimal ratio has been here evidenced on low temperature processable AZO. Consequently, it would be relevant to extend the presented study to other device architectures.

We proposed a one-step scalable perovskite process, with an AZO sublayer deposited at low temperature. These architectures have led to interesting results. However, in order to develop its potential, further studies are still needed. They should consist of optimizing the global device architecture and expanding this study to other perovskite formulations.

**Supplementary Materials:** Supplements on photovoltaic, infrared, titration and perovskite state data are available online at <http://www.mdpi.com/1996-1073/13/8/1927/s1>. Figure S1. (a) Typical potentiometric titration curve (example for PK 2-1); (b) Table for the calculation of equivalent volumes and chloride contents. Figure S2. Representative JV curves of AZO-based PV cells realized using different perovskite precursors compositions. Figure S3. Photographs of the perovskite layers according to the different precursors ratio. (scale bar: 0.5 cm). Figure S4. SEM images of (a) the AZO sub-layer (top view), (b) a representative MAPbI<sub>3-x</sub>Cl<sub>x</sub> perovskite layer (top view), (c) the cross-section of an AZO based half-cell (examples for 3-1 precursors' ratio). Figure S5. Photographs of a perovskite layer (example for 3-1 precursors' ratio): showing the influence of the annealing time (100 °C) on the perovskite formation and decomposition when deposited on the AZO ETL underlying layer presented in this work. Table S1. Peaks assignments of IR spectra. All wavenumbers are given in cm<sup>-1</sup>.

**Author Contributions:** Conceptualization, L.P., E.P. and M.M.; methodology, L.P., E.P. and M.M.; validation, L.P., E.P. and M.M., S.B. and L.F.; formal analysis, M.S.; investigation, M.S., L.P., E.P. and M.M.; data curation, M.S., L.P., E.P. and M.M.; writing—original draft preparation, M.S., L.P., E.P. and M.M.; writing—review and editing, L.P., E.P., M.M., S.B. and L.F. All authors have read and agreed to the published version of the manuscript.

**Funding:** This work was financed by the Conseil Savoie Mont Blanc, University Savoie Mont Blanc, and Commissariat à l'énergie atomique et aux énergies alternatives. This work was performed within the framework of the Center of Excellence of Multifunctional Architected Materials (CEMAM) n°AN-10-LABEX-44-01.

**Acknowledgments:** Vanson Nguyen from CEA/LHET is gratefully acknowledged for SKP measurements on ETL layers. We express our gratitude to Sungmin Diana Kim from Case Western Reserve University for her careful reading of this article, and correction of the English.

**Conflicts of Interest:** There are no conflicts to declare.

## References

1. Stranks, S.D.; Eperon, G.E.; Grancini, G.; Menelaou, C.; Alcocer, M.J.P.; Leijtens, T.; Herz, L.M.; Petrozza, A.; Snaith, H.J. Electron-Hole Diffusion Lengths Exceeding 1 micrometer in an organometal trihalide Perovskite Absorber. *Science* **2013**, *342*, 341–344. [[CrossRef](#)]
2. Sum, T.C.; Mathews, N. Advancements in perovskite solar cells: Photophysics behind the photovoltaics. *Energy Environ. Sci.* **2014**, *7*, 2518–2534. [[CrossRef](#)]
3. National Renewable Energy Laboratory (NREL). *Best Research-Cell Efficiencies*; National Renewable Energy Laboratory (NREL): Golden, CO, USA, 2019.
4. Wang, Q.; Lyu, M.; Zhang, M.; Yun, J.-H.; Chen, H.; Wang, L. Transition from the Tetragonal to Cubic Phase of Organohalide Perovskite: The Role of Chlorine in Crystal Formation of CH<sub>3</sub>NH<sub>3</sub>PbI<sub>3</sub> on TiO<sub>2</sub> Substrates. *J. Phys. Chem. Lett.* **2015**, *6*, 4379–4384. [[CrossRef](#)] [[PubMed](#)]
5. Kim, H.S.; Lee, C.R.; Im, J.H.; Lee, K.B.; Moehl, T.; Marchioro, A.; Moon, S.J.; Humphry-Baker, R.; Yum, J.H.; Moser, J.E.; et al. Lead iodide perovskite sensitized all-solid-state submicron thin film mesoscopic solar cell with efficiency exceeding 9%. *Sci. Rep.* **2012**, *2*, 591. [[CrossRef](#)] [[PubMed](#)]
6. Chen, Q.; Zhou, H.; Hong, Z.; Luo, S.; Duan, H.S.; Wang, H.H.; Liu, Y.; Li, G.; Yang, Y. Planar heterojunction perovskite solar cells via vapor-assisted solution process. *J. Am. Chem. Soc.* **2014**, *136*, 622–625. [[CrossRef](#)]
7. Tao, C.; Neutzner, S.; Colella, L.; Marras, S.; Srimath Kandada, A.R.; Gandini, M.; De Bastiani, M.; Pace, G.; Manna, L.; Caironi, M.; et al. 17.6% Stabilized Efficiency in Low-Temperature Processed Planar Perovskite Solar Cells. *Energy Environ. Sci.* **2015**, *8*, 2365–2370. [[CrossRef](#)]

8. Saliba, M.; Correa-Baena, J.P.; Wolff, C.M.; Stolterfoht, M.; Phung, N.; Albrecht, S.; Neher, D.; Abate, A. How to Make over 20% Efficient Perovskite Solar Cells in Regular (n-i-p) and Inverted (p-i-n) Architectures. *Chem. Mater.* **2018**, *30*, 4193–4201. [\[CrossRef\]](#)
9. Mahmood, K.; Swain, B.S.; Amassian, A. 16.1% Efficient Hysteresis-Free Mesoporous Perovskite Solar Cells Based on Synergistically Improved ZnO Nanorod Arrays. *Adv. Energy Mater.* **2015**, *5*, 1–11. [\[CrossRef\]](#)
10. Pang, Z.; Sun, Y.; Gao, Y.; Zhang, X.; Sun, Y.; Yang, J. Unravelling the mechanism of interface passivation engineering for achieving high-efficient ZnO-based planar perovskite solar cells. *J. Power Sources* **2019**, *438*, 226957. [\[CrossRef\]](#)
11. Spalla, M.; Planes, E.; Perrin, L.; Matheron, M.; Berson, S.; Flandin, L. Alternative Electron Transport Layer Based on Al-Doped ZnO and SnO<sub>2</sub> for Perovskite Solar Cells: Impact on Microstructure and Stability. *ACS Appl. Energy Mater.* **2019**, *2*, 7183–7195. [\[CrossRef\]](#)
12. Planes, E.; Spalla, M.; Juillard, S.; Perrin, L.; Flandin, L. Absolute Quantification of Photo-/Electroluminescence Imaging for Solar Cells: Definition and Application to Organic and Perovskite Devices. *ACS Appl. Electron. Mater.* **2019**, *1*, 2489–2501. [\[CrossRef\]](#)
13. Liu, D.; Wang, Y.; Xu, H.; Zheng, H.; Zhang, T.; Zhang, P.; Wang, F.; Wu, J.; Wang, Z.; Chen, Z.; et al. SnO<sub>2</sub>-Based Perovskite Solar Cells: Configuration Design and Performance Improvement. *Sol. RRL* **2019**, *3*, 1800292. [\[CrossRef\]](#)
14. Jiang, Q.; Zhang, X.; You, J. SnO<sub>2</sub>: A Wonderful Electron Transport Layer for Perovskite Solar Cells. *Small* **2018**, *14*, 1801154. [\[CrossRef\]](#) [\[PubMed\]](#)
15. Xiong, L.; Guo, Y.; Wen, J.; Liu, H.; Yang, G.; Qin, P.; Fang, G. Review on the Application of SnO<sub>2</sub> in Perovskite Solar Cells. *Adv. Funct. Mater.* **2018**, *28*, 1802757. [\[CrossRef\]](#)
16. Yang, J.; Siempelkamp, B.D.; Mosconi, E.; De Angelis, F.; Kelly, T.L. Origin of the Thermal Instability in CH<sub>3</sub>NH<sub>3</sub>PbI<sub>3</sub> Thin Films Deposited on ZnO. *Chem. Mater.* **2015**, *27*, 4229–4236. [\[CrossRef\]](#)
17. Seo, S.; Jeong, S.; Bae, C.; Park, N.G.; Shin, H. Perovskite Solar Cells with Inorganic Electron- and Hole-Transport Layers Exhibiting Long-Term ( $\approx$ 500 h) Stability at 85 °C under Continuous 1 Sun Illumination in Ambient Air. *Adv. Mater.* **2018**, *30*, 1–8. [\[CrossRef\]](#)
18. Baltakesmez, A.; Biber, M.; Tüzemen, S. Inverted planar perovskite solar cells based on Al doped ZnO substrate. *J. Radiat. Res. Appl. Sci.* **2017**, *11*, 124–129. [\[CrossRef\]](#)
19. Tseng, Z.L.; Chiang, C.H.; Chang, S.H.; Wu, C.G. Surface engineering of ZnO electron transporting layer via Al doping for high efficiency planar perovskite solar cells. *Nano Energy* **2016**, *28*, 311–318. [\[CrossRef\]](#)
20. Chouhan, A.S.; Jasti, N.P.; Avasthi, S. Surface Modification of Aluminum Doped Zinc Oxide by Ozone-Gas Treatment for Perovskite Solar Cells. In Proceedings of the nanoGe International Conference on Perovskite Solar Cells, Photonics and Optoelectronics (NIPHO19), Jerusalem, Israel, 24–27 February 2019. [\[CrossRef\]](#)
21. Wu, S.H.; Lin, M.Y.; Chang, S.H.; Tu, W.C.; Chu, C.W.; Chang, Y.C. A Design Based on a Charge-Transfer Bilayer as an Electron Transport Layer for Improving the Performance and Stability in Planar Perovskite Solar Cells. *J. Phys. Chem. C* **2018**, *122*, 236–244. [\[CrossRef\]](#)
22. Zhao, X.; Shen, H.; Zhang, Y.; Li, X.; Zhao, X.; Tai, M.; Li, J.; Li, J.; Li, X.; Lin, H. Aluminum-Doped Zinc Oxide as Highly Stable Electron Collection Layer for Perovskite Solar Cells. *ACS Appl. Mater. Interfaces* **2016**, *8*, 7826–7833. [\[CrossRef\]](#)
23. Dong, Q.; Ho, C.H.Y.; Yu, H.; Salehi, A.; So, F. Defect Passivation by Fullerene Derivative in Perovskite Solar Cells with Aluminum-doped Zinc Oxide as Electron Transporting Layer. *Chem. Mater.* **2019**, *31*, 6833–6840. [\[CrossRef\]](#)
24. Matsui, T.; Yokoyama, T.; Negami, T.; Sekiguchi, T.; Saliba, M.; Grätzel, M.; Segawa, H. Effect of rubidium for thermal stability of triple-cation perovskite solar cells. *Chem. Lett.* **2018**, *47*, 814–816. [\[CrossRef\]](#)
25. Saliba, M.; Matsui, T.; Seo, J.Y.; Domanski, K.; Correa-Baena, J.P.; Nazeeruddin, M.K.; Zakeeruddin, S.M.; Tress, W.; Abate, A.; Hagfeldt, A.; et al. Cesium-containing triple cation perovskite solar cells: Improved stability, reproducibility and high efficiency. *Energy Environ. Sci.* **2016**, *9*, 1989–1997. [\[CrossRef\]](#) [\[PubMed\]](#)
26. Zimmermann, I.; Gratia, P.; Martineau, D.; Grancini, G.; Audinot, J.N.; Wirtz, T.; Nazeeruddin, M.K. Improved efficiency and reduced hysteresis in ultra-stable fully printable mesoscopic perovskite solar cells through incorporation of CuSCN into the perovskite layer. *J. Mater. Chem. A* **2019**, *7*, 8073–8077. [\[CrossRef\]](#)
27. Yu, H.; Wang, F.; Xie, F.; Li, W.; Chen, J.; Zhao, N. The Role of Chlorine in the Formation Process of “CH<sub>3</sub>NH<sub>3</sub>PbI<sub>3</sub>-xCl<sub>x</sub>” Perovskite. *Adv. Funct. Mater.* **2014**, *24*, 7102–7108. [\[CrossRef\]](#)

28. Li, Z.; Kolodziej, C.; McCleese, C.; Wang, L.; Kovalsky, A.; Samia, A.C.; Zhao, Y.; Burda, C. Effect of chloride substitution on interfacial charge transfer processes in MAPbI<sub>3</sub> perovskite thin film solar cells: Planar versus mesoporous. *Nanoscale Adv.* **2019**, *1*, 827–833. [\[CrossRef\]](#)
29. Xie, F.X.; Su, H.; Mao, J.; Wong, K.S.; Choy, W.C.H. Evolution of diffusion length and trap state induced by chloride in perovskite solar cell. *J. Phys. Chem. C* **2016**, *120*, 21248–21253. [\[CrossRef\]](#)
30. De Quilletes, D.W.; Vorpahl, S.M.; Stranks, S.D.; Nagaoka, H.; Eperon, G.E.; Ziffer, M.E.; Snaith, H.J.; Ginger, D.S. Impact of micro structure on local carrier lifetime in perovskite solar cells. *Sci. Rep.* **2015**, *348*, 683–686.
31. Fan, L.; Ding, Y.; Luo, J.; Shi, B.; Yao, X.; Wei, C.; Zhang, D.; Wang, G.; Sheng, Y.; Chen, Y.; et al. Elucidating the role of chlorine in perovskite solar cells. *J. Mater. Chem. A* **2017**, *5*, 7423–7432. [\[CrossRef\]](#)
32. Colella, S.; Mosconi, E.; Fedeli, P.; Listorti, A.; Gazza, F.; Orlandi, F.; Ferro, P.; Besagni, T.; Rizzo, A.; Calestani, G.; et al. MAPbI<sub>3</sub>-xCl<sub>x</sub> mixed halide perovskite for hybrid solar cells: The role of chloride as dopant on the transport and structural properties. *Chem. Mater.* **2013**, *25*, 4613–4618. [\[CrossRef\]](#)
33. Colella, S.; Mosconi, E.; Pellegrino, G.; Alberti, A.; Guerra, V.L.P.; Masi, S.; Listorti, A.; Rizzo, A.; Condorelli, G.G.; De Angelis, F.; et al. Elusive presence of chloride in mixed halide perovskite solar cells. *J. Phys. Chem. Lett.* **2014**, *5*, 3532–3538. [\[CrossRef\]](#) [\[PubMed\]](#)
34. Park, B.W.; Zhang, X.; Johansson, E.M.J.; Hagfeldt, A.; Boschloo, G.; Seok, S., II; Edvinsson, T. Analysis of crystalline phases and integration modelling of charge quenching yields in hybrid lead halide perovskite solar cell materials. *Nano Energy* **2017**, *40*, 596–606. [\[CrossRef\]](#)
35. Tombe, S.; Adam, G.; Heilbrunner, H.; Yumusak, C.; Apaydin, D.H.; Hailegnaw, B.; Ulbricht, C.; Arendse, C.J.; Langhals, H.; Iwuohaa, E.; et al. The influence of perovskite precursor composition on the morphology and photovoltaic performance of mixed halide MAPbI<sub>3</sub>-xCl<sub>x</sub> solar cells. *Sol. Energy* **2018**, *163*, 215–223. [\[CrossRef\]](#)
36. Mehdi, H.; Mhamdi, A.; Bouazizi, A. Effect of perovskite precursor ratios and solvents volume on the efficiency of MAPbI<sub>3</sub>-xCl<sub>x</sub> mixed halide perovskite solar cells. *Mater. Sci. Semicond. Process.* **2020**, *109*, 104915. [\[CrossRef\]](#)
37. Kleinschmidt, A.T.; Root, S.E.; Lipomi, D.J. Poly(3-hexylthiophene) (P3HT): Fruit fly or outlier in organic solar cell research? *J. Mater. Chem. A* **2017**, *5*, 11396–11400. [\[CrossRef\]](#)
38. Heo, J.H.; Im, S.H.; Noh, J.H.; Mandal, T.N.; Lim, C.-S.; Chang, J.A.; Lee, Y.H.; Kim, H.; Sarkar, A.; Nazeeruddin, M.K.; et al. Efficient inorganic–organic hybrid heterojunction solar cells containing perovskite compound and polymeric hole conductors. *Nat. Photonics* **2013**, *7*, 486–491. [\[CrossRef\]](#)
39. Spalla, M.; Perrin, L.; Planes, E.; Matheron, M.; Berson, S.; Flandin, L. Effect of the Hole Transporting/Active Layer Interface on the Perovskite Solar Cell Stability. *ACS Appl. Energy Mater.* **2020**. [\[CrossRef\]](#)
40. Yaghoobi Nia, N.; Lamanna, E.; Zendejdel, M.; Palma, A.L.; Zurlo, F.; Castriotta, L.A.; Di Carlo, A. Doping Strategy for Efficient and Stable Triple Cation Hybrid Perovskite Solar Cells and Module Based on Poly(3-hexylthiophene) Hole Transport Layer. *Small* **2019**, *15*, 1904399. [\[CrossRef\]](#)
41. Calió, L.; Kazim, S.; Grätzel, M.; Ahmad, S. Hole-Transport Materials for Perovskite Solar Cells. *Angew. Chem. Int. Ed.* **2016**, *55*, 14522–14545.
42. Qin, P.; Tanaka, S.; Ito, S.; Tetreault, N.; Manabe, K.; Nishino, H.; Nazeeruddin, M.K.; Grätzel, M. Inorganic hole conductor-based lead halide perovskite solar cells with 12.4% conversion efficiency. *Nat. Commun.* **2014**, *5*, 3834. [\[CrossRef\]](#)
43. Jena, A.K.; Numata, Y.; Ikegami, M.; Miyasaka, T. Role of spiro-OMeTAD in performance deterioration of perovskite solar cells at high temperature and reuse of the perovskite films to avoid Pb-waste. *J. Mater. Chem. A* **2018**, *6*, 2219–2230. [\[CrossRef\]](#)
44. Wang, G.; Swensen, J.; Moses, D.; Heeger, A.J. Increased mobility from regioregular poly(3-hexylthiophene) field-effect transistors. *J. Appl. Phys.* **2003**, *93*, 6137–6141. [\[CrossRef\]](#)
45. Jung, E.H.; Jeon, N.J.; Park, E.Y.; Moon, C.S.; Shin, T.J.; Yang, T.-Y.; Noh, J.H.; Seo, J. Efficient, stable and scalable perovskite solar cells using poly(3-hexylthiophene). *Nature* **2019**, *567*, 511–515. [\[CrossRef\]](#) [\[PubMed\]](#)
46. Nia, N.Y.; Matteocci, F.; Cina, L.; Di Carlo, A. High-Efficiency Perovskite Solar Cell Based on Poly(3-Hexylthiophene): Influence of Molecular Weight and Mesoscopic Scaffold Layer. *ChemSusChem* **2017**, *10*, 3854–3860. [\[CrossRef\]](#)
47. Williams, S.T.; Zuo, F.; Chueh, C.C.; Liao, C.Y.; Liang, P.W.; Jen, A.K.Y. Role of chloride in the morphological evolution of organo-lead halide perovskite thin films. *ACS Nano* **2014**, *8*, 10640–10654. [\[CrossRef\]](#)

48. Tidhar, Y.; Edri, E.; Weissman, H.; Zohar, D.; Hodes, G.; Cahen, D.; Rybtchinski, B.; Kirmayer, S. Crystallization of methyl ammonium lead halide perovskites: Implications for photovoltaic applications. *J. Am. Chem. Soc.* **2014**, *136*, 13249–13256. [\[CrossRef\]](#)
49. Stone, K.H.; Gold-Parker, A.; Pool, V.L.; Unger, E.L.; Bowring, A.R.; McGehee, M.D.; Toney, M.F.; Tassone, C.J. Transformation from crystalline precursor to perovskite in PbCl<sub>2</sub>-derived MAPbI<sub>3</sub>. *Nat. Commun.* **2018**, *9*, 3458. [\[CrossRef\]](#)
50. Eperon, G.E.; Burlakov, V.M.; Docampo, P.; Goriely, A.; Snaith, H.J. Morphological control for high performance, solution-processed planar heterojunction perovskite solar cells. *Adv. Funct. Mater.* **2014**, *24*, 151–157. [\[CrossRef\]](#)
51. Unger, E.L.; Bowring, A.R.; Tassone, C.J.; Pool, V.L.; Gold-Parker, A.; Cheacharoen, R.; Stone, K.H.; Hoke, E.T.; Toney, M.F.; McGehee, M.D. Chloride in lead chloride-derived organo-metal halides for perovskite-absorber solar cells. *Chem. Mater.* **2014**, *26*, 7158–7165. [\[CrossRef\]](#)
52. Li, Y.; Sun, W.; Yan, W.; Ye, S.; Peng, H.; Liu, Z.; Bian, Z.; Huang, C. High-Performance Planar Solar Cells Based on CH<sub>3</sub>NH<sub>3</sub>PbI<sub>3</sub>-xCl<sub>x</sub> Perovskites with Determined Chlorine Mole Fraction. *Adv. Funct. Mater.* **2015**, *25*, 4867–4873. [\[CrossRef\]](#)
53. Nenon, D.P.; Christians, J.A.; Wheeler, L.M.; Blackburn, J.L.; Sanehira, E.M.; Dou, B.; Olsen, M.L.; Zhu, K.; Berry, J.J.; Luther, J.M. Structural and chemical evolution of methylammonium lead halide perovskites during thermal processing from solution. *Energy Environ. Sci.* **2016**, *9*, 2072–2082. [\[CrossRef\]](#)
54. Shen, D.; Yu, X.; Cai, X.; Peng, M.; Ma, Y.; Su, X.; Xiao, L.; Zou, D. Understanding the solvent-assisted crystallization mechanism inherent in efficient organic-inorganic halide perovskite solar cells. *J. Mater. Chem. A* **2014**, *2*, 20454–20461. [\[CrossRef\]](#)
55. Dong, H.; Pang, S.; Zhang, Y.; Chen, D.; Zhu, W.; Xi, H.; Chang, J.; Zhang, J.; Zhang, C.; Hao, Y. Improving Electron Extraction Ability and Device Stability of Perovskite Solar Cells Using a Compatible PCBM/AZO Electron Transporting Bilayer. *Nanomaterials* **2018**, *8*, 720. [\[CrossRef\]](#) [\[PubMed\]](#)
56. Uddin, A.; Mahmud, M.A.; Elumalai, N.K.; Wang, D.; Upama, M.B.; Wright, M.; Chan, K.H.; Haque, F.; Xu, C. Perovskite solar cells for roll-to-roll fabrication. *Renew. Energy Environ. Sustain.* **2017**, *2*, 7. [\[CrossRef\]](#)
57. Galatopoulos, F.; Papadas, I.T.; Armatas, G.S.; Choulis, S.A. Long Thermal Stability of Inverted Perovskite Photovoltaics Incorporating Fullerene-Based Diffusion Blocking Layer. *Adv. Mater. Interfaces* **2018**, *5*, 1800280. [\[CrossRef\]](#)
58. Arai, R.; Furukawa, S.; Sato, N.; Yasuda, T. Organic energy-harvesting devices achieving power conversion efficiencies over 20% under ambient indoor lighting. *J. Mater. Chem. A* **2019**, *7*, 20187–20192. [\[CrossRef\]](#)
59. Savva, A.; Papadas, I.T.; Tsikritzis, D.; Ioakeimidis, A.; Galatopoulos, F.; Kapnisis, K.; Fuhrer, R.; Hartmeier, B.; Osajca, M.F.; Luechinger, N.A.; et al. Inverted Perovskite Photovoltaics Using Flame Spray Pyrolysis Solution Based CuAlO<sub>2</sub>/Cu–O Hole-Selective Contact. *ACS Appl. Energy Mater.* **2019**, *2*, 2276–2287. [\[CrossRef\]](#)
60. Nam, S.; Vu, T.K.; Le, D.T.; Oh, I. Low-Temperature Solution Process of Al-Doped ZnO Nano-flakes for Flexible Perovskite Solar Cells. *J. Electrochem. Sci. Technol.* **2018**, *9*, 118–125. [\[CrossRef\]](#)
61. Ganapathy, V.; Karunakaran, B.; Rhee, S.W. Improved performance of dye-sensitized solar cells with TiO<sub>2</sub>/alumina core-shell formation using atomic layer deposition. *J. Power Sources* **2010**, *195*, 5138–5143. [\[CrossRef\]](#)
62. Heo, J.H.; Im, S.H. CH<sub>3</sub>NH<sub>3</sub>PbI<sub>3</sub>/poly-3-hexylthiophen perovskite mesoscopic solar cells: Performance enhancement by Li-assisted hole conduction. *Phys. Status Solidi Rapid Res. Lett.* **2014**, *8*, 816–821. [\[CrossRef\]](#)
63. Liu, D.; Gangishetty, M.K.; Kelly, T.L. Effect of CH<sub>3</sub>NH<sub>3</sub>PbI<sub>3</sub> thickness on device efficiency in planar heterojunction perovskite solar cells. *J. Mater. Chem. A* **2014**, *2*, 19873–19881. [\[CrossRef\]](#)
64. Zhou, P.; Bu, T.; Shi, S.; Li, L.; Zhang, Y.; Ku, Z.; Peng, Y.; Zhong, J.; Cheng, Y.-B.; Huang, F. Efficient and stable mixed perovskite solar cells using P3HT as a hole transporting layer. *J. Mater. Chem. C* **2018**, *6*, 5733–5737. [\[CrossRef\]](#)
65. Wang, W.; Xu, H.; Cai, J.; Zhu, J.; Ni, C.; Hong, F.; Fang, Z.; Xu, F.; Cui, S.; Xu, R.; et al. Visible blind ultraviolet photodetector based on CH<sub>3</sub>NH<sub>3</sub>PbCl<sub>3</sub> thin film. *Opt. Express* **2016**, *24*, 8411–8419. [\[CrossRef\]](#) [\[PubMed\]](#)
66. Eze, V.O.; Lei, B.; Mori, T. Air-assisted flow and two-step spin-coating for highly efficient CH<sub>3</sub>NH<sub>3</sub>PbI<sub>3</sub> perovskite solar cells. *Jpn. J. Appl. Phys.* **2016**, *55*, 02BF08. [\[CrossRef\]](#)
67. Xu, F.; Zhang, T.; Li, G.; Zhao, Y. Synergetic Effect of Chloride Doping and CH<sub>3</sub>NH<sub>3</sub>PbCl<sub>3</sub> on CH<sub>3</sub>NH<sub>3</sub>PbI<sub>3</sub>-xCl<sub>x</sub> Perovskite-Based Solar Cells. *ChemSusChem* **2017**, *10*, 2365–2369. [\[CrossRef\]](#)



68. Sun, Y.; Chen, H.; Zhang, T.; Wang, D. Chemical state of chlorine in perovskite solar cell and its effect on the photovoltaic performance. *J. Mater. Sci.* **2018**, *53*, 13976–13986. [[CrossRef](#)]
69. Ono, L.K.; Raga, S.R.; Remeika, M.; Winchester, A.J.; Gabe, A.; Qi, Y. Pinhole-free hole transport layers significantly improve the stability of MAPbI<sub>3</sub>-based perovskite solar cells under operating conditions. *J. Mater. Chem. A* **2015**, *3*, 15451–15456. [[CrossRef](#)]
70. Saliba, M.; Correa-Baena, J.-P.; Grätzel, M.; Hagfeldt, A.; Abate, A. Perovskite Solar Cells: From the Atomic Level to Film Quality and Device Performance. *Angew. Chem. Int. Ed.* **2018**, *57*, 2554–2569. [[CrossRef](#)] [[PubMed](#)]
71. Wei-Guang, D.E.; Chao-Yu, C.P. *Perovskite Solar Cells: Principle, Materials And Devices*; World Scie.: Singapore, 2017.
72. McLeod, J.A.; Wu, Z.; Sun, B.; Liu, L. The influence of the I/Cl ratio on the performance of CH<sub>3</sub>NH<sub>3</sub>PbI<sub>3</sub>-xCl<sub>x</sub>-based solar cells: Why is CH<sub>3</sub>NH<sub>3</sub>I: PbCl<sub>2</sub> = 3:1 the “magic” ratio? *Nanoscale* **2016**, *8*, 6361–6368. [[CrossRef](#)] [[PubMed](#)]
73. Chen, S.; Yu, X.; Cai, X.; Peng, M.; Yan, K.; Dong, B.; Hu, H.; Chen, B.; Gao, X.; Zou, D. PbCl<sub>2</sub>-assisted film formation for high-efficiency heterojunction perovskite solar cells. *RSC Adv.* **2015**, *6*, 648–655. [[CrossRef](#)]
74. Liang, P.W.; Liao, C.Y.; Chueh, C.C.; Zuo, F.; Williams, S.T.; Xin, X.K.; Lin, J.; Jen, A.K.Y. Additive enhanced crystallization of solution-processed perovskite for highly efficient planar-heterojunction solar cells. *Adv. Mater.* **2014**, *26*, 3748–3754. [[CrossRef](#)] [[PubMed](#)]
75. Poglitsch, A.; Weber, D. Dynamic disorder in methylammoniumtrihalogenoplumbates (II) observed by millimeter-wave spectroscopy. *J. Chem. Phys.* **1987**, *87*, 6373–6378. [[CrossRef](#)]
76. Maculan, G.; Sheikh, A.D.; Abdelhady, A.L.; Saidaminov, M.I.; Haque, M.A.; Murali, B.; Alarousu, E.; Mohammed, O.F.; Wu, T.; Bakr, O.M. CH<sub>3</sub>NH<sub>3</sub>PbCl<sub>3</sub> Single Crystals: Inverse Temperature Crystallization and Visible-Blind UV-Photodetector. *J. Phys. Chem. Lett.* **2015**, *6*, 3781–3786. [[CrossRef](#)] [[PubMed](#)]
77. Baikie, T.; Fang, Y.; Kadro, J.M.; Schreyer, M.; Wei, F.; Mhaisalkar, S.G.; Graetzel, M.; White, T.J. Synthesis and crystal chemistry of the hybrid perovskite (CH<sub>3</sub>NH<sub>3</sub>)PbI<sub>3</sub> for solid-state sensitised solar cell applications. *J. Mater. Chem. A* **2013**, *1*, 5628. [[CrossRef](#)]
78. Oku, T. Crystal Structures of CH<sub>3</sub>NH<sub>3</sub>PbI<sub>3</sub> and Related Perovskite Compounds Used for Solar Cells. In *Solar Cells—New Approaches and Reviews*; Kosyachenko, L.A., Ed.; InTech: Rijeka, Croatia, 2015.
79. Mosconi, E.; Ronca, E.; De Angelis, F. First-principles investigation of the TiO<sub>2</sub>/organohalide perovskites interface: The role of interfacial chlorine. *J. Phys. Chem. Lett.* **2014**, *5*, 2619–2625. [[CrossRef](#)] [[PubMed](#)]
80. Pham, N.D.; Tiong, V.T.; Chen, P.; Wang, L.; Wilson, G.J.; Bell, J.; Wang, H. Enhanced perovskite electronic properties via a modified lead(ii) chloride Lewis acid-base adduct and their effect in high-efficiency perovskite solar cells. *J. Mater. Chem. A* **2017**, *5*, 5195–5203. [[CrossRef](#)]
81. Mosconi, E.; Amat, A.; Nazeeruddin, M.K.; Grätzel, M.; De Angelis, F. First-principles modeling of mixed halide organometal perovskites for photovoltaic applications. *J. Phys. Chem. C* **2013**, *117*, 13902–13913. [[CrossRef](#)]
82. Xing, G.; Mathews, N.; Lim, S.S.; Lam, Y.M.; Mhaisalkar, S.; Sum, T.C. Long-Range Balanced Electron- and Hole-Transport Lengths in Organic-Inorganic CH<sub>3</sub>NH<sub>3</sub>PbI<sub>3</sub>. *Science* **2013**, *342*, 344–347. [[CrossRef](#)]
83. Park, B.W.; Philippe, B.; Gustafsson, T.; Sveinbjörnsson, K.; Hagfeldt, A.; Johansson, E.M.J.; Boschloo, G. Enhanced crystallinity in organic-inorganic lead halide perovskites on mesoporous TiO<sub>2</sub> via disorder-order phase transition. *Chem. Mater.* **2014**, *26*, 4466–4471. [[CrossRef](#)]
84. Ledinský, M.; Löper, P.; Niesen, B.; Holovský, J.; Moon, S.J.; Yum, J.H.; De Wolf, S.; Fejfar, A.; Ballif, C. Raman spectroscopy of organic-inorganic halide perovskites. *J. Phys. Chem. Lett.* **2015**, *6*, 401–406.
85. Zhou, Y.; Garces, H.F.; Padture, N.P. Challenges in the ambient Raman spectroscopy characterization of methylammonium lead triiodide perovskite thin films. *Front. Optoelectron.* **2016**, *9*, 81–86. [[CrossRef](#)]
86. Cabana, A.; Sandorfy, C. The infrared spectra of solid methylammonium halides. *Spectrochim. Acta* **1962**, *18*, 843–861. [[CrossRef](#)]
87. Glaser, T.; Müller, C.; Sendner, M.; Krekeler, C.; Semonin, O.E.; Hull, T.D.; Yaffe, O.; Owen, J.S.; Kowalsky, W.; Pucci, A.; et al. Infrared Spectroscopic Study of Vibrational Modes in Methylammonium Lead Halide Perovskites. *J. Phys. Chem. Lett.* **2015**, *6*, 2913–2918. [[CrossRef](#)] [[PubMed](#)]
88. Idígoras, J.; Todinova, A.; Sánchez-Valencia, J.R.; Barranco, A.; Borrás, A.; Anta, J.A. The interaction between hybrid organic-inorganic halide perovskite and selective contacts in perovskite solar cells: An infrared spectroscopy study. *Phys. Chem. Chem. Phys.* **2016**, *18*, 13583–13590.

89. Pérez-Osorio, M.A.; Milot, R.L.; Filip, M.R.; Patel, J.B.; Herz, L.M.; Johnston, M.B.; Giustino, F. Vibrational Properties of the Organic-Inorganic Halide Perovskite  $\text{CH}_3\text{NH}_3\text{PbI}_3$  from Theory and Experiment: Factor Group Analysis, First-Principles Calculations, and Low-Temperature Infrared Spectra. *J. Phys. Chem. C* **2015**, *119*, 25703–25718.
90. Kumar, M.H.; Yantara, N.; Dharani, S.; Graetzel, M.; Boix, P.P.; Mathews, N. Flexible, low-temperature, solution processed ZnO-based perovskite solid state solar cells. *Chem. Commun.* **2013**, *49*, 11089–11091. [[CrossRef](#)]



© 2020 by the authors. Licensee MDPI, Basel, Switzerland. This article is an open access article distributed under the terms and conditions of the Creative Commons Attribution (CC BY) license (<http://creativecommons.org/licenses/by/4.0/>).